Supporting Materials: Effects of macroH2A and H2A.Z on nucleosome structure and dynamics as elucidated by molecular dynamics simulations

Samuel Bowerman and Jeff Wereszczynski*

Department of Physics and Center for Molecular Study of Condensed Soft Matter

Illinois Institute of Technology

Chicago, IL 60616, USA

*Corresponding author: jwereszc@iit.edu

1 Methods

1.1 System Construction and Simulation Details

The canonical nucleosome was initiated from the crystal structure of Davey *et al.* (PDB ID: 1KX5),[1] which includes the protruding N-terminal tails (except for the initial three residues of each H2B histone). The crystallographic Mn^{2+} were replaced by physiological Mg^{2+}. Additional Mg^{2+} ions were added to fill symmetrically suggested voids. The crystallographic waters were also maintained. The L1-Mutant structure was then created from the canonical one by mutating the ^{38}NYAE^{41} H2A L1 loops to ^{38}HPKY^{41} sequence of macroH2A. The mutation was done using VMD. The macroH2A system was initialized from the crystal structure solved by Chakravarthy *et al.* (PDB ID: 1U35).[2] The missing tail segments were constructed using the canonical structure as a reference. Strong similarities in DNA arrangement - particularly at DNA-protein binding sites (Figure S1) - allowed for the 146 base pairs of DNA from the crystal structure to be replaced by the 147 bp (plus Mg^{2+}) of the 1KX5 structure, and sequence divergent residues were mutated to match the sequence of the 1KX5 system. These actions were taken to ensure that differences between the systems were attributable only to H2A sequence divergence. The H2A.Z system was constructed analogously, using the crystal structure of Suto *et al.* (PDB ID: 1F66).[3] Therefore, each system was composed of 147 palindromic base pairs of α-satellite DNA wrapped around a histone core of *Xenopus laevis* H3, H4, and H2B with human H2A histones and variants. Histidine states were assigned using PROPKA and the interactive H-Bond Optimizer of the Desmond-Schrödinger package.[4]

Each system was simulated three times. Each simulation underwent 10,000 steps of geometric minimization (5,000 steps with protein heavy atoms harmonically restrained by a force constant of 10 kcal/mol/Å^2 and 5,000 steps without restraints). Heating was done by gradually raising the temperature from 10 to 300 K over 6 ps of simulation in the NVT ensemble. During heating, protein heavy atoms were harmonically restrained with a force constant of 10 kcal/mol/Å^2. The restraints were then gradually released over 600ps in the NPT ensemble.[5] Each simulation was then conducted for an additional 250ns in the NPT ensemble using a Langevin piston with a 100 fs period and collision frequency of 3 ps^{-1}. The SHAKE algorithm was used to allow for a 2 fs timestep, and long-range electrostatics were calculated using the particle mesh Ewald method.[6,7] Short range interactions were calculated with a 10 Å cutoff, where a switching function was applied at 8 Å. It was observed that ∼50ns was required for system equilibration (Figures S3-S6), and so ∼200ns of production data was obtained from each simulation (600ns per system) for analysis. For reference, one simulation could achieve a speed of ∼20ns per day on 256 processors on the XSEDE supercomputer Stampede, resulting in a cumulative cost of approximately 921,000 CPU hours.

Similarly, the 147bp of linear DNA was constructed in a 150mM NaCl box of TIP3P water, extending 10 Å from the solute. Following minimization and heating, three separate simulations were conducted in the NPT ensemble for an additional 60 ns. The initial 10ns of simulation were required for the RMSD to equilibrate, so only the last 50ns of each simulation was used during the MMGBSA analysis (150ns total). These simulations achieved similar speeds as the nucleosome simulations, requiring an additional 56,000 CPU hours (cumulative total of 976,296 hours).

1.2 Quantification of Equilibration Differences

To ensure that the modifications to the variant nucleosomes did not have a large effect on their equilibration dynamics, a separate trajectory was produced for the 1F66 H2A.Z nucleosome ("1F66 with tails"). In this system, the only modification to the crystal structure as the addition of histone tails. This structure was minimized and equilibrated analogously to the 250ns simulations, but the NPT simulation following heating was conducted for 50ns instead of the full 250ns. Equilibration times were determined by observing the backbone RMSD of the systems and by tail compaction (Figure S2A). Furthermore, the sampling differences between the 1F66 with tails simulation and the three 250ns simulations were compared against the inter-simulation differences of the 250ns set via the Kullback-Leibler Divergence of dihedral angle sampling. Local flexibility differences were compared via the "Mean Fluctuation Difference (MFD)." This metric measures the average difference of residue RMSF values of a target simulation (the "wild-type") against a reference set (the three 250ns simulations):

$$MFD = \frac{1}{N_s} \sum_{s=1}^{N_s} \left(\sum_{i=1}^{N_{residues}} [RMSF(i)_{wild-type} - RMSF(i)_s] \right) \quad (1)$$

where N_s is equal to 3, for the three 250ns simulations. In order to create a consistent sampling space for all comparison measurements, the three 250ns H2A.Z simulations were concatenated to include only the first 50ns.

1.3 MM/GBSA Analysis

It is important to note that the MM/GBSA approach is typically done in one of two ways: the single trajectory and the three-trajectory methods. In the single trajectory approach, the complex is separated into receptor and ligand components using coordinates produced in the complex assembly simulation. In the three-trajectory approach, the coordinates for analysis are taken from three separately simulated states (complex, receptor only, and ligand only). The three-trajectory approach supposes that the ligand and receptor components exist in substantially different conformations when separated from one another. For the nucleosome, this is clearly true for supercoiled DNA,[8] but is unclear for the histone core. However, the crystal structure of the octamer, *sans* DNA, still shows the colloquial histone fold, albeit under 2M salt concentration.[9] Furthermore, the free energy of construction for the octamer ($\Delta G_{octamer}$) — calculated using an MM/GBSA analysis on the extracted coordinates — was approximately -200 kcal/mol across all four systems, suggesting that the octamer core is stable on the hundreds of nanoseconds timescales that we are capable of observing. It is also worth noting that simulation costs are strongly affected by the number of atoms, which is primarily dictated by the size of the octamer in nucleosome simulations. Thus, separate simulations of each octamer system would effectively double the simulation cost with little payoff in the accessible timescales. Therefore, a hybrid, two-trajectory approach was taken in which protein coordinates were extracted from the nucleosome assembly for each separate system while simulating a separate set of coordinates for the DNA (which could be applied against all four systems).

1.4 Allosteric Calculations

Residue correlations were calculated using the "largest linear mutual information" method.[10,11] In this method, the linear mutual information is calculated between all heavy atoms in the system. The residue-wise mutual information values were converted to a Pearson correlation coefficient-like value by $r_{i,j} = [1 - e^{(-2I_{i,j}/3)}]^{1/2}$, where $I_{i,j}$ is the largest linear mutual information between any two atoms of the residues i and j.

Contact maps were produced in-house using the MDAnalysis package.[12] Two residues were considered to be in contact if their C_α (protein) or C1' (nucleic) atoms were within 10 Å for 70% of the configurations. Using the predefined correlation matrices and this contact map, a NetworkX edgelist was formed.[13] The length of each edge was defined by $D_{i,j} = -log(r_{i,j})$, where $r_{i,j}$ is the correlation value between residues i and j. The optimal paths were calculated using the NetworkX implementation of Dijkstra's algorithm, and the sub-optimal paths were determined using Yen's K-Shortest Paths algorithm.

The Kullback-Leibler Divergence of dihedral angles were calculated using the method of McClendon.[14] In this method, each simulation was separated into three blocks (9 blocks per system) with 31,666 configurations (roughly 63.3 ns) per block. Histogram widths were 15 degrees. The Kullback-Leibler Divergence values were calculated for each variant by using the populations of the canonical system as a reference set. Bootstrapping techniques were employed to calculate the self-divergence of the canonical system. For any residue in a variant system whose divergence value was below this self-divergence threshold, the KL-Divergence value for that residue was set to 0.

1.5 Edge-betweenness Centrality

The importance of a node in a communication network can be defined by its edge-betweenness centrality.[15] In this method, the "shortest" correlation pathway between all residue-pairs is calculated. A residue's edge-betweenness centrality is then defined as the number of shortest paths in which the residue appears:

$$C(i) = \frac{1}{N} \sum_{s \neq t \neq i} x_i\,(s,t) \tag{2}$$

where N is the total number of paths and $x_i(s,t)$ is either 0 (residue i does not exist in path between residues s and t) or 1 (residue i does exist in said path). For visualization purposes, centrality values are normalized such that the minimum centrality is 0 and the maximum centrality is 1, according to the formula:

$$C_{norm}\,(i) = \frac{C(i) - C_{min}}{C_{max} - C_{min}} \tag{3}$$

where C_{max} and C_{min} are the maximum and minimum centrality values in the network.

From the plot of normalized centrality value vs percentile (Figure S11), we observe that the difference in centrality between percentile increments is not constant but is large at the upper and lower quartiles and steady in the interquartile region. The inflection point of the upper quartile exists near the tenth percentile, so we have chosen this location as our cut-off

for defining allosteric "hotspots."

We were able to identify several well-known post-translational modifications (PTMs) in the canonical nucleosome by our betweenness centrality measurement.[16–18] In the canonical system, we observe 6 of 23 mononucleosome altering PTM sites (monoNCP PTMs) in the upper tenth percentile and 12 of 23 in the upper quartile. The significance of observing this subset of residues in each percentile was tested by calculating the pmf of a hypergeometric distribution,[19]

$$\mathrm{pmf}\,(x = k) = \frac{\binom{K}{k}\binom{N-K}{n-k}}{\binom{N}{n}} \tag{4}$$

where N is the total number of protein residues (487), n is the percentile population size (n=49 for the upper tenth, and n=122 for the upper quartile), K is the total number of monoNCP PTM residues (23), and k is the number of observed monoNCP PTM sites (k=6 for the upper tenth, and k=12 for the upper quartile). Using these values, the upper tenth percentile observation has a p-value of 0.0155, and the upper quartile p-value is 0.00288. Therefore, the observation that monoNCP PTMs are located at allosteric hotspots is statistically significant.

Furthermore, we can quantify the presence of monoNCP PTMs at allosteric hotspots by calculating the enrichment factor (EF) of monoNCP PTMs over random selection,

$$EF = \frac{k}{K}\frac{N}{n} \tag{5}$$

where the variables have the same meaning as for the hypergeometric distribution. We then calculate an EF of 2.54 for monoNCP PTM presence at allosteric hotspots. A plot of EF vs centrality percentile can be found in Figure S13.

2 Equilibration Comparison

The equilibration time for the 1F66 with tails simulation was measured via backbone RMSD values and histone tail compaction, and it was found to be in agreement with the three production H2A.Z simulations (Figure S2A-B). Furthermore, the MFD values obtained by comparing the 1F66 with tails simulation against the set of three production simulations show that local fluctuation differences are comparable to the inter-simulation average for the production set (Figure S2C). In this metric, the fluctuations in the histone core and DNA are less than 1 Å, on average, while the histone tails exhibit a wider deviation in fluctuations. These values are consistent with the noise present in comparing the fluctuations between the set of H2A.Z production simulations. Lastly, individual residue sampling was compared using the Kullback-Leibler Divergence of dihedral angle sampling. From these calculations, the average divergence value between the 1F66 with tails simulation and the three 250ns simulations was 0.596 (σ=1.06). The residue-averaged Kullback-Leibler divergence value for comparisons between each of the 250ns was 0.531 (σ=1.03), showing that the differences in local sampling of the 1F66 with tails simulation and the three 250ns simulations was comparable to the noise between simulations of identical systems.

References

[1] Davey,C.A., Sargent,D.F.; Luger,K., Maeder,A.W. and Richmond,T.J. Solvent Mediated Interactions in the Structure of the Nucleosome Core Particle at 1.9Å Resolution. *J. Mol. Biol.* **2002**, *319*, 1097 – 1113.

[2] Chakravarthy,S., Gundimella,S.K., Caron,C., Perche,P.Y., Pehrson,J.R., Khochbin,S. and Luger,K. Structural characterization of the histone variant macroH2A. *Mol. Cell. Biol.* **2005**, *25*, 7616–7624.

[3] Suto,R.K., Clarkson,M.J., Tremethick,D.J. and Luger,K. Crystal structure of a nucleosome core particle containing the variant histone H2A.Z. *Nat. Struct. Biol.* **2000**, *7*, 1121–1124.

[4] Olsson,M. H.M., Søndergaard,C.R., Rostkowski,M. and Jensen,J.H. PROPKA3: Consistent Treatment of Internal and Surface Residues in Empirical pKa Predictions. *J. Chem. Theor. Comp.* **2011**, *7*, 525–537.

[5] Feller,S.E., Zhang,Y.H., Pastor,R.W. and Brooks,B.R. Constant-pressure molecular-dynamics simulation - the langevin piston method. *J. Chem. Phys.* **1995**, *103*, 4613–4621.

[6] Ryckaert,J.P., Ciccotti,G. and Berendsen,H.J. Numerical integration of the cartesian equations of motion of a system with constraints: molecular dynamics of n-alkanes. *J. Comp. Phys.* **1977**, *23*, 327 – 341.

[7] Darden,T., York,D. and Pedersen,L. Particle mesh Ewald: An N log (N) method for Ewald sums in large systems. *J. Chem. Phys.* **1993**, *98*, 10089–10092.

[8] Bishop, T.C. Molecular dynamics simulations of a nucleosome and free DNA. *J. Biomol. Struct. Dyn.* **2005**, *22*, 673–686.

[9] Wood,C.M., Nicholson, J.M., Lambert, S.J., Chantalat, L., Reynolds, C.D., and Baldwin,J.P. High-resolution structure of the native histone octamer. *Acta Crystallogr. F* **2005**, *61*, 541–545.

[10] Lange,O.F. and Grubmuller,H. Generalized correlation for biomolecular dynamics. *Proteins* **2006**, *62*, 1053–1061.

[11] Scarabelli,G. and Grant,B.J. Kinesin-5 allosteric inhibitors uncouple the dynamics of nucleotide, microtubule, and neck-linker binding sites. *Biophys. J.* **2014**, *107*, 2204–2213.

[12] Michaud-Agrawal,N., Denning,E., Woolf,T. and Beckstein,O. MDAnalysis: A Toolkit for the Analysis of Molecular Dynamics Simulations. *J. Comp. Chem.* **2011**, *32*, 2319–2327.

[13] Hagberg,A.A., Schult,D.A. and Swart,P.J. Exploring network structure, dynamics, and function using NetworkX. Proceedings of the 7th Python in Science Conference (SciPy2008). Pasadena, CA USA, 2008, pp 11–15.

[14] McClendon,C.L., Hua,L., Barreiro,A. and Jacobson,M.P. Comparing Conformational Ensembles Using the Kullback-Leibler Divergence Expansion. *J. Chem. Theor. Comp.* **2012**, *8*, 2115–2126.

[15] Brandes,U. A faster algorithm for betweenness centrality. *J. Math. Sociol.* **2001**, *25*, 163–177.

[16] Bowman,G.D. and Poirier,M.G. Post-translational modifications of histones that influence nucleosome dynamics. *Chem. Rev.* **2015**, *115*, 2274–2295.

[17] Khare,S.P., Habib,F., Sharma,R., Gadewal,N., Gupta,S., and Galande,S. HIstome–a relational knowledgebase of human histone proteins and histone modifying enzymes. *Nucl. Acids Res.* **2012**, *40*, D337–342.

[18] Hornbeck,P.V., Kornhauser,J.M., Tkachev,S., Zhang,B., Skrzypek,E., Murray,B., Latham,V. and Sullivan,M. PhosphoSitePlus: a comprehensive resource for investigating the structure and function of experimentally determined post-translational modifications in man and mouse. *Nucl. Acids Res.* **2012**, *40*, D261–270.

[19] Rice,J.A. *Mathematical Statistics and Data Analysis*, 3rd ed., Duxbury Press: Belmont, CA, 2007.

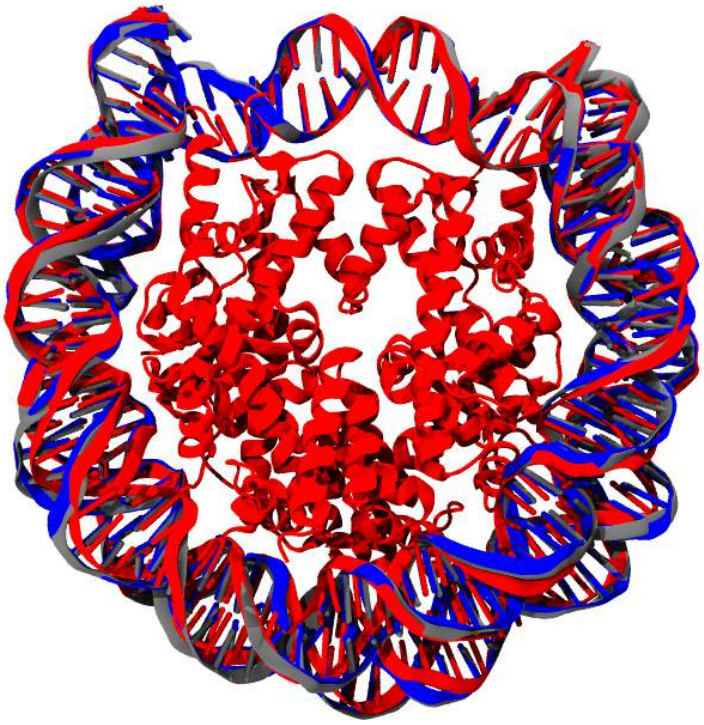

Figure S1: Comparison of crystallographic DNA arrangment in the canonical (blue), macroH2A (red), and H2A.Z (grey) nucleosomes. As expected, the DNA-histone binding sites show strong agreement in coordination between the three structures.

System	H2A R^{29}-DNA	H2B S^{33}-DNA	L1-L1	Dimer-tetramer
Canonical NCP	63%	40%	0.5 ± 0.1	14.8 ± 1.1
L1 Mutant	70%	60%	0.4 ± 0.1	16.5 ± 1.0
macroH2A NCP	52%	30%	0.2 ± 0.1	14.7 ± 0.8
H2A.Z NCP	73%	85%	0.1 ± 0.1	14.4 ± 1.1

Table S1: Hydrogen bonding at key locations in the nucleosome. For the H-Bonds formed with the DNA, the occupancy of each bond is given. For the other interactions, the average number of hydrogen bonds between each group in a given frame is listed.

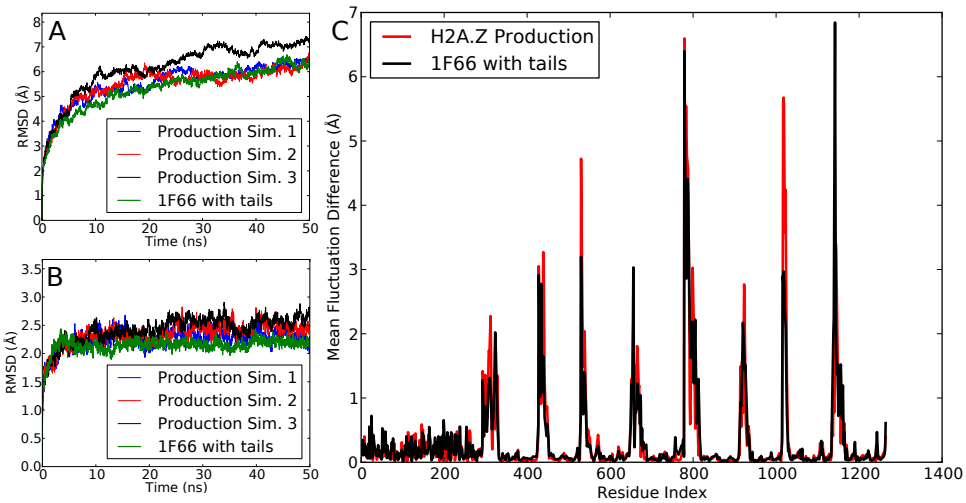

Figure S2: Backbone RMSD timeseries for (A) the whole system and (B) the nucleosome core, including DNA. Displayed are the three production simulations of H2A.Z (blue,red,black), as well as the 50ns 1F66 with tails simulation (green). The 1F66 with tails simulation shows no change in required equilibration time. (C) per-Residue Mean Fluctuation Difference (MFD) plotted for the 1F66 with tails simulation referenced against the set of three production simulations (black). With the exception of the histone tails, the MFD of the 1F66 with tails simulation differs less than 1 Å from the production runs of H2A.Z. This is comparable to the noise present when comparing the three different production simulations of H2A.Z (red).

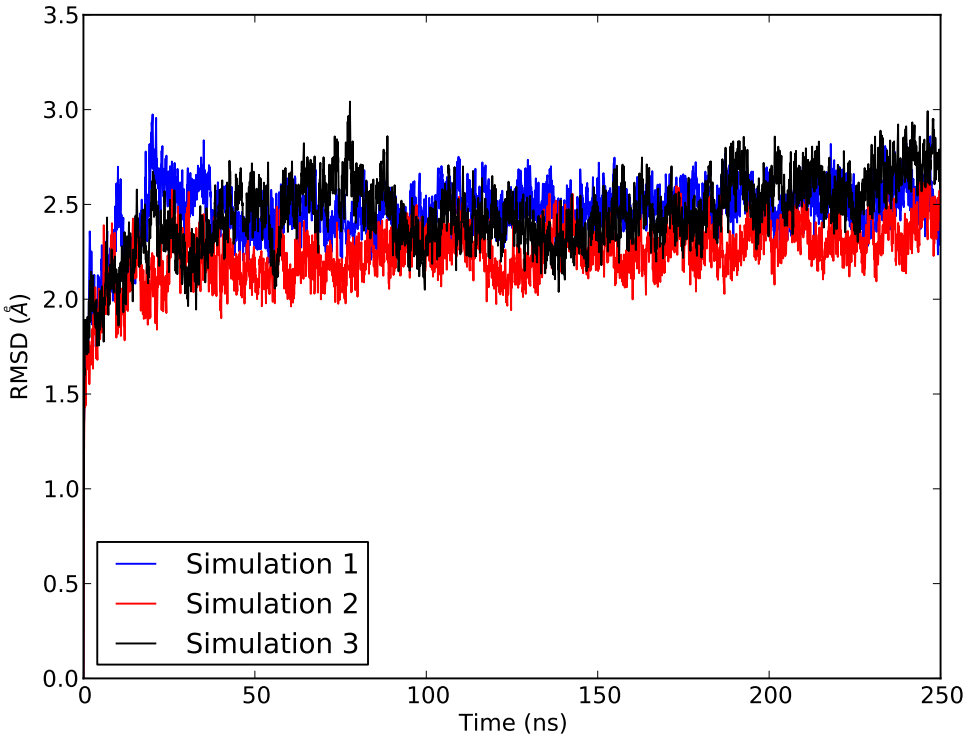

Figure S3: Backbone RMSD of three canonical simulations. The simulations were fit to the histone core backbone, and the RMSD calculations were done on the DNA and histone core backbone atoms, excluding tail residues.

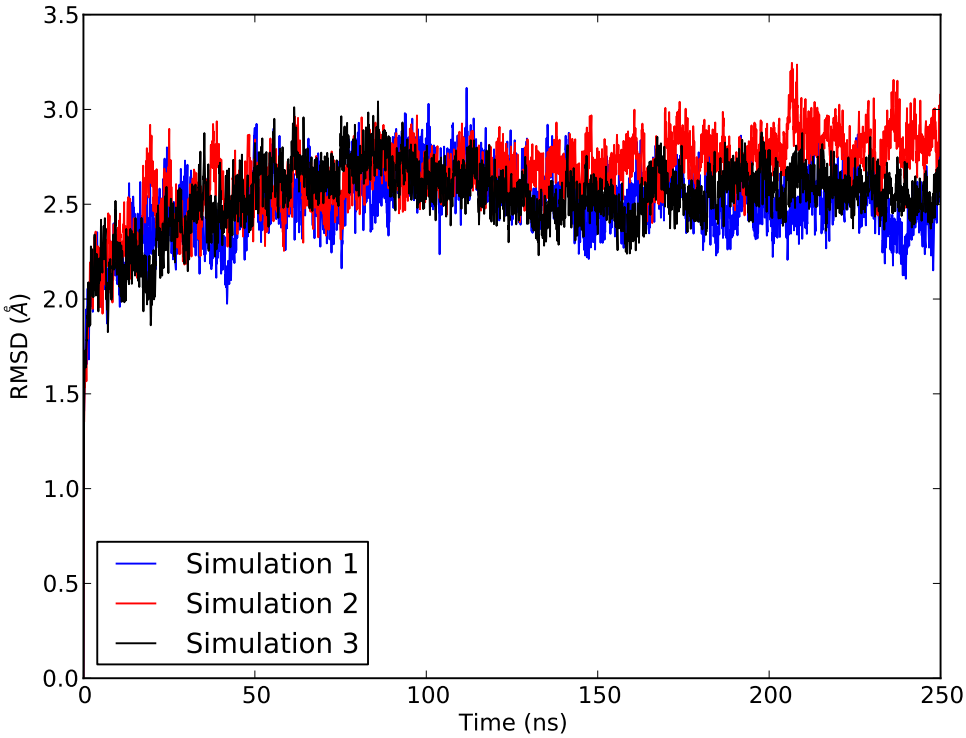

Figure S4: Backbone RMSD of three L1-Mutant simulations. The simulations were fit to the histone core backbone, and the RMSD calculations were done on the DNA and histone core backbone atoms, excluding tail residues.

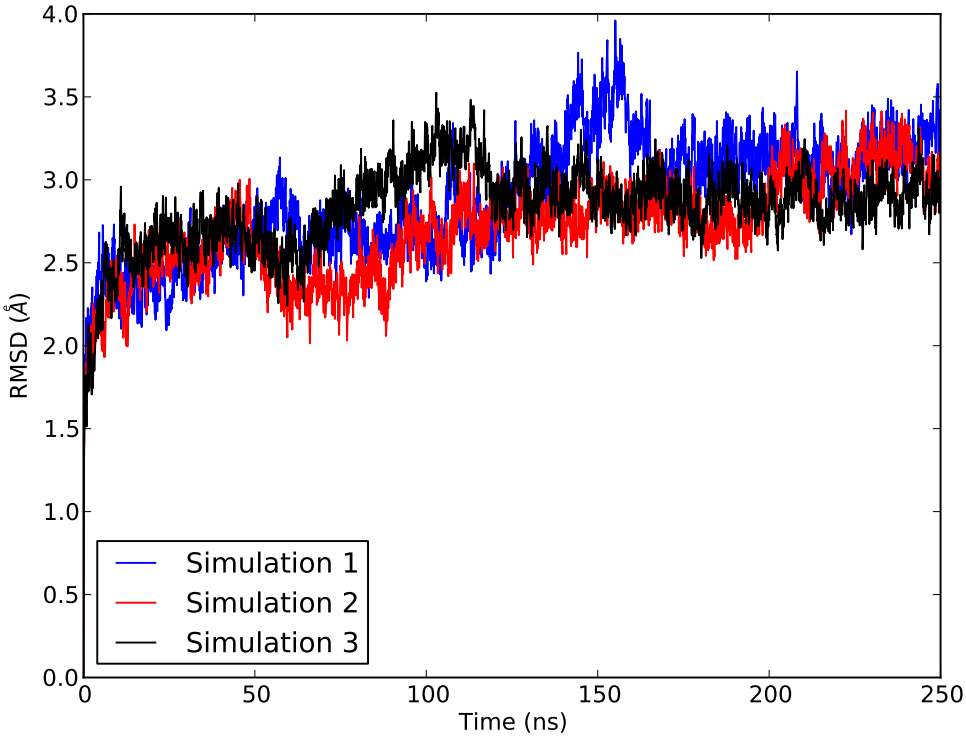

Figure S5: Backbone RMSD of three macroH2A simulations. The simulations were fit to the histone core backbone, and the RMSD calculations were done on the DNA and histone core backbone atoms, excluding tail residues.

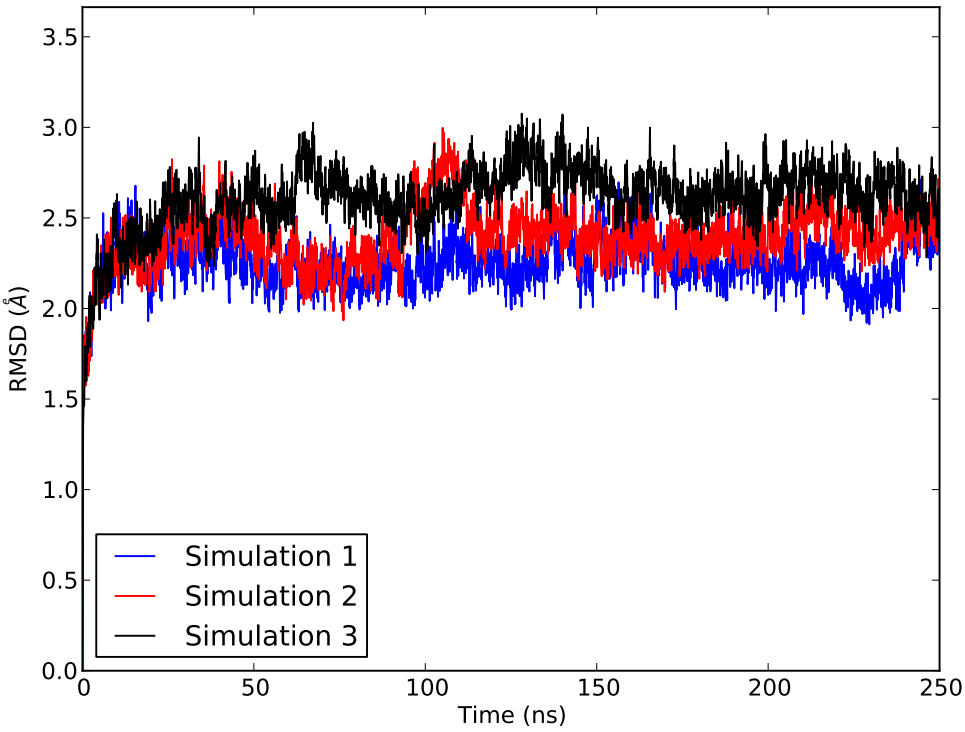

Figure S6: Backbone RMSD of three H2A.Z simulations. The simulations were fit to the histone core backbone, and the RMSD calculations were done on the DNA and histone core backbone atoms, excluding tail residues.

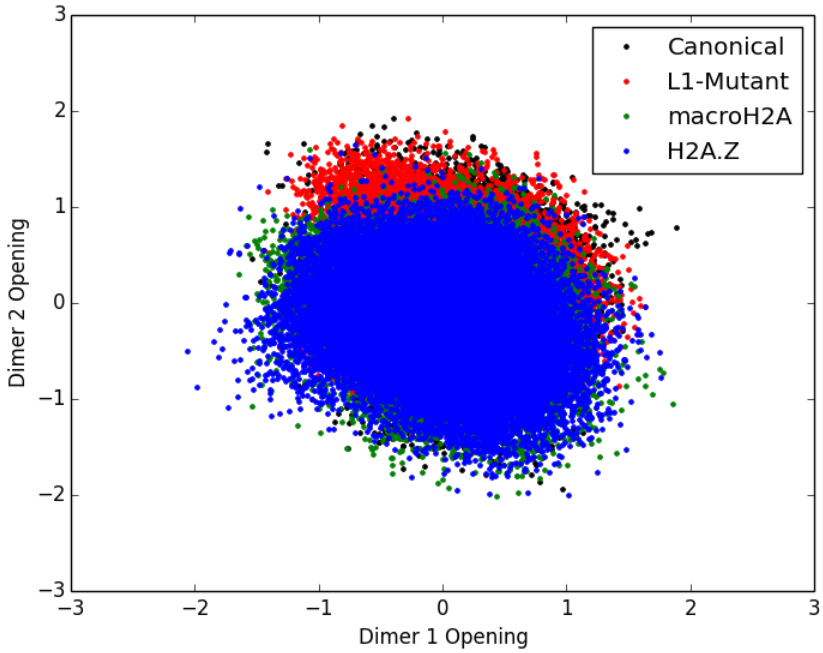

Figure S7: Dimer dissociation phase space for the nucleosome systems. All systems sample the same region of this space, which suggests that H2A composition has little effect on dimer dissociation in the hundreds of nanoseconds timescale. For reference, the dimer separation event occurs on the millisecond timescale.

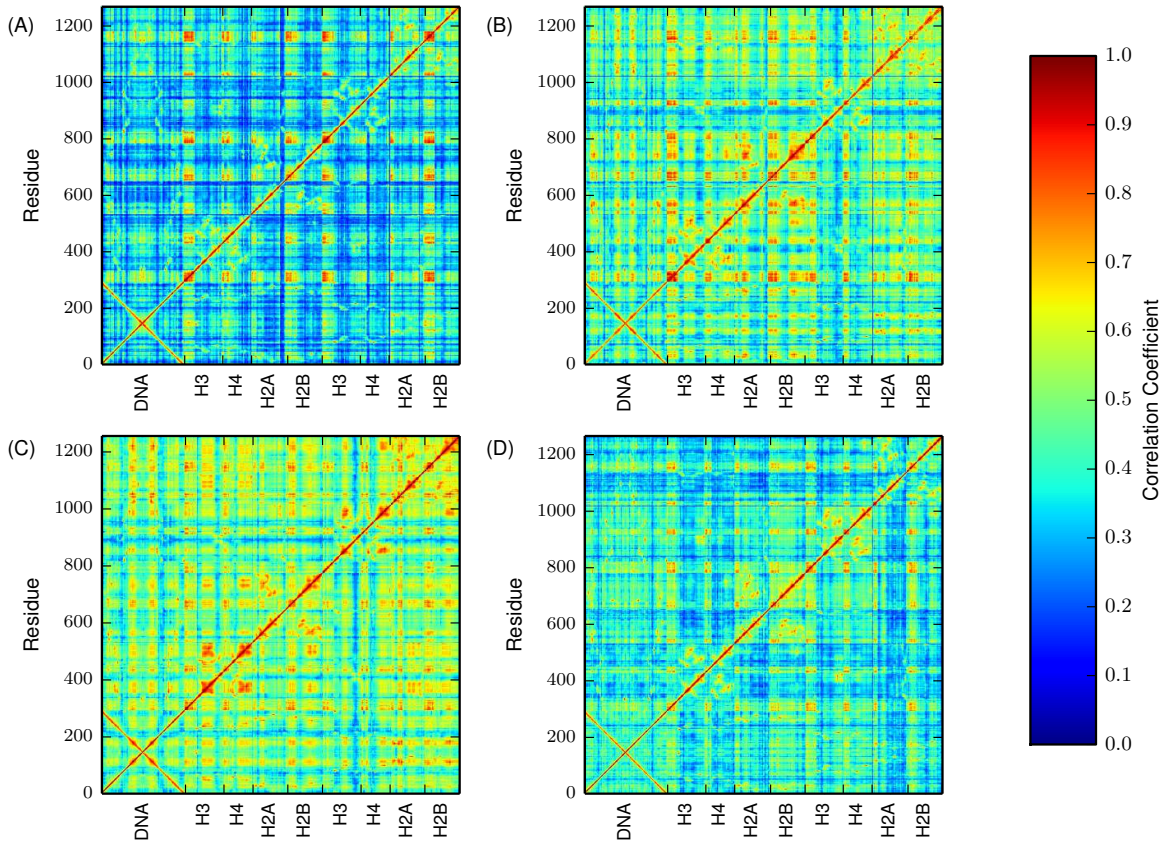

Figure S8: Pearsified Largest Linear Mutual Information matrices for (a) canonical, (b) L1-Mutant, (c) macroH2A, and (d) H2A.Z nucleosomes. The canonical NCP shows the weakest average correlation across the whole molecule, and the macroH2A variant shows the strongest. The L1-Mutant correlation strengths are similar to macroH2A, while the H2A.Z nucleosome shows correlations that are slightly above the levels of the canonical nucleosome. The steady increase in correlations within the variant systems is likely a result of favorable changes in interhistone interactions.

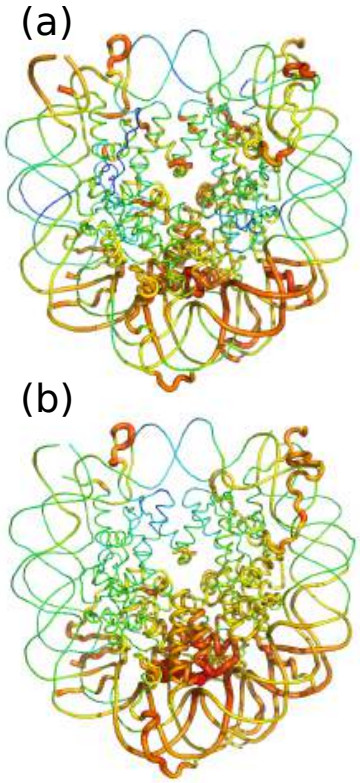

Figure S9: Average individual residue correlation with L1 loop residues for (a) canonical and (b) L1-Mutant nucleosomes. Thicker, redder residues are those with stronger average correlations with the L1 loop sequence. The L1-Mutant nucleosome shows increased correlations near the L1-L1 interface, as well as among H2B-H4 four helix bundle residues. Both systems display appreciable correlations between the L1 loops and docking domain residues in the dimer and tetramer. Histone tails were truncated to improve clarity.

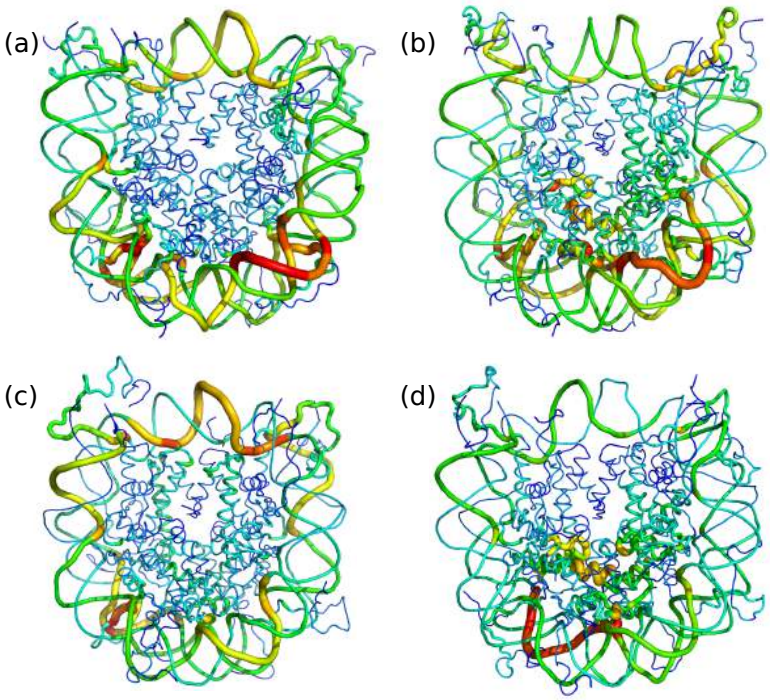

Figure S10: Edge-betweenness centrality for (a) canonical, (b) L1-Mutant, (c) H2A.Z, and (d) macroH2A nucleosomes. Brighter, wider regions represent locations that are accessed more frequently in the optimal communication pathways of each nucleosome system. The H2A L1-L1 interaction region in the L1-Mutant and macroH2A systems act as communication hubs for allosteric networks in the nucleosome, whereas the canonical and H2A.Z nucleosomes rely heavier on DNA to propagate information.

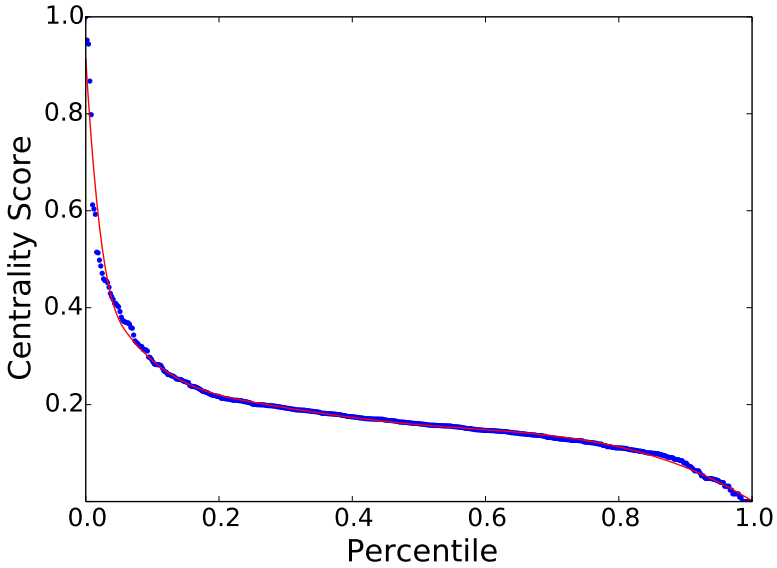

Figure S11: Centrality scores vs percentile ranking (blue dots) for the canonical nucleosome. The spline fit is represented in red. The drastic change in centrality score in the upper quartile indicates that residues rely heavily on several key residues for information propagation. The inflection point of this trend is located at the tenth percentile.

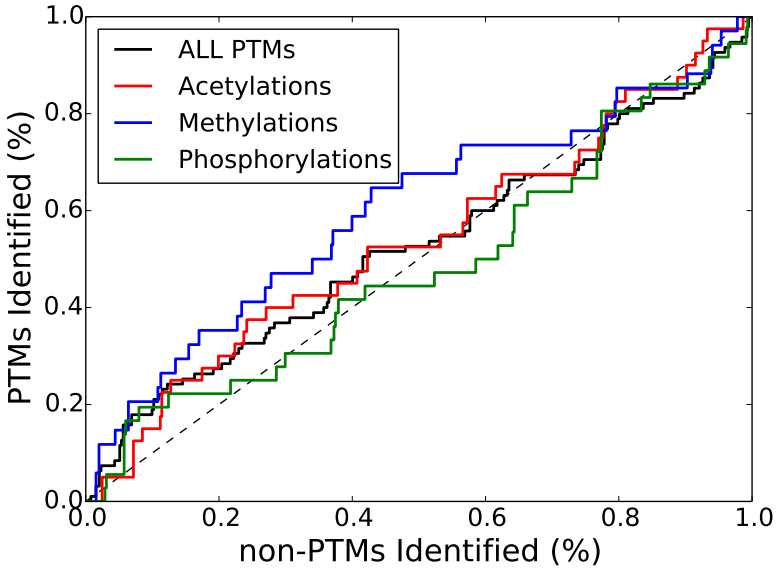

Figure S12: ROC plot for the canonical nucleosome with PTMs separated by modification type. Methylations exist most prevalently as allosteric hotspots, and acetylations are the least prevalent. The early enrichment of methylations is a result of their presence near DNA extremities and between superhelical DNA turns where pathways cross the symmetries.

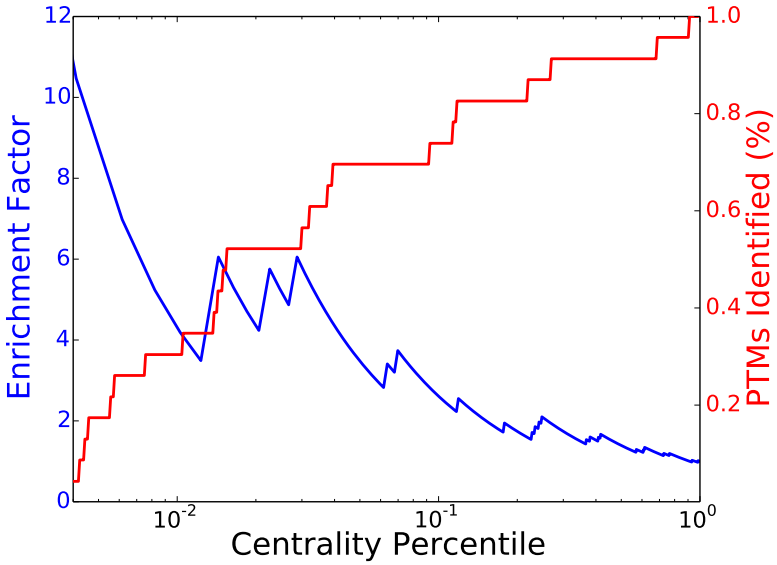

Figure S13: Enrichment Factor (blue) and monoNCP PTM identification percent (red) as functions of centrality percentile in the canonical nucleosome. We observe a strong degree of early enrichment for identifying monoNCP PTMs at allosteric hotspots. At the cutoff of the tenth percentile, we observe an EF of 2.54.

Table S2: Protein-normalized centrality values for the 23 monoNCP PTM targets. The percentile rank of each value is also listed. The residues in the upper quartile are listed in bold. Those in the upper tenth percentile are italicized. PTM sites that have significantly smaller centrality values than neighboring sequence residues in the upper quartile are labeled by an (*) and the value of the neighbor is reported.

	Canonical		L1-Mutant		macroH2A		H2A.Z	
PTM	Centrality	Percentile	Centrality	Percentile	Centrality	Percentile	Centrality	Percentile
H3 K4me3	0.05	6.6	0.07	6.3	0.05	6.2	0.06	6.7
H3 K9ac	0.13	27.0	0.19	22.6	0.14	24.8	0.16	27.5
H3 K14ac	0.20	**75.6**	0.30	51.0	0.23	53.4	0.26	61.2
H3 K18ac	0.27	**87.9**	0.39	73.9	0.30	69.8	0.34	**78.4**
H3 K23ac	0.34	***92.8***	0.51	**87.3**	0.38	**82.0**	0.44	**88.9**
H3 K36me2,3	0.47	***97.5***	0.80	***97.3***	0.45	**86.1**	0.69	***97.7***
H3 Y41ph	0.46	***96.9***	1.00	***100.0***	0.67	***96.9***	0.84	***99.8***
H3 R42me2a	0.51	***98.4***	0.79	***96.7***	0.37	**81.5**	0.79	***99.2***
H3 T45ph*	0.29	**75.0**	0.38	71.1	0.22	52.4	0.28	67.0
H3 K56ac	0.17	58.9	0.18	20.1	0.22	52.4	0.19	35.6
H3 S57ph	0.15	39.0	0.16	17.9	0.22	52.4	0.16	28.6
H3 K64ac	0.15	42.7	0.26	38.0	0.27	63.6	0.21	46.1
H3 K115ac	0.15	38.4	0.13	11.7	0.06	8.5	0.24	53.9
H3 T118ph	0.37	***93.4***	0.43	**81.9**	0.14	25.8	0.63	***96.5***
H3 K122ac	0.23	**81.9**	0.29	47.4	0.13	23.9	0.39	**82.7**
H4 K16ac	0.21	**77.0**	0.38	70.0	0.16	33.9	0.18	34.2
H4 S47ph*	0.25	**85.4**	0.28	43.9	0.19	44.3	0.34	**78.2**
H4 K77ac	0.18	61.8	0.29	45.2	0.15	28.3	0.25	58.0
H4 K79ac*	0.31	***91.4***	0.34	63.8	0.56	***95.0***	0.35	**79.8**
H4 K91ac	0.12	23.4	0.38	70.0	0.57	***95.4***	0.29	68.9
H4 R92me	0.21	**76.4**	0.53	**88.5**	0.81	***99.4***	0.33	**77.6**
H2B K30ar	0.94	***99.6***	0.81	***97.7***	0.26	62.4	0.72	***98.8***
H2B K123ub1	0.00	0.0	0.00	0.0	0.00	0.0	0.00	0.0

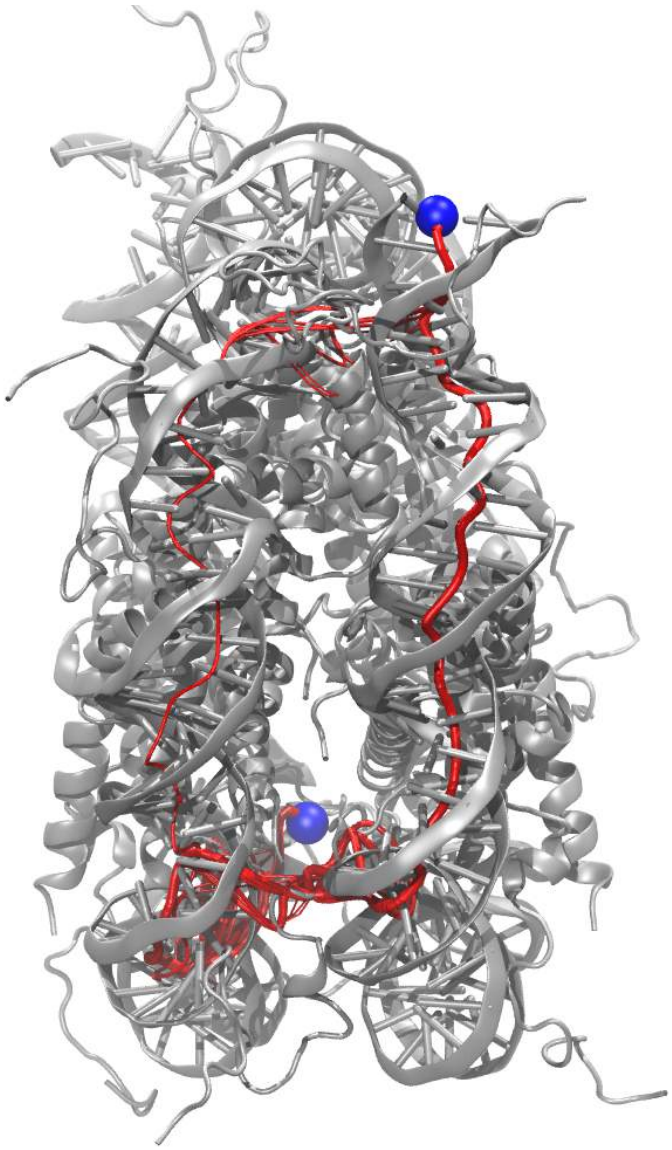

Figure S14: Sub-optimal pathways for L1 loop to DNA exit in the canonical nucleosome.

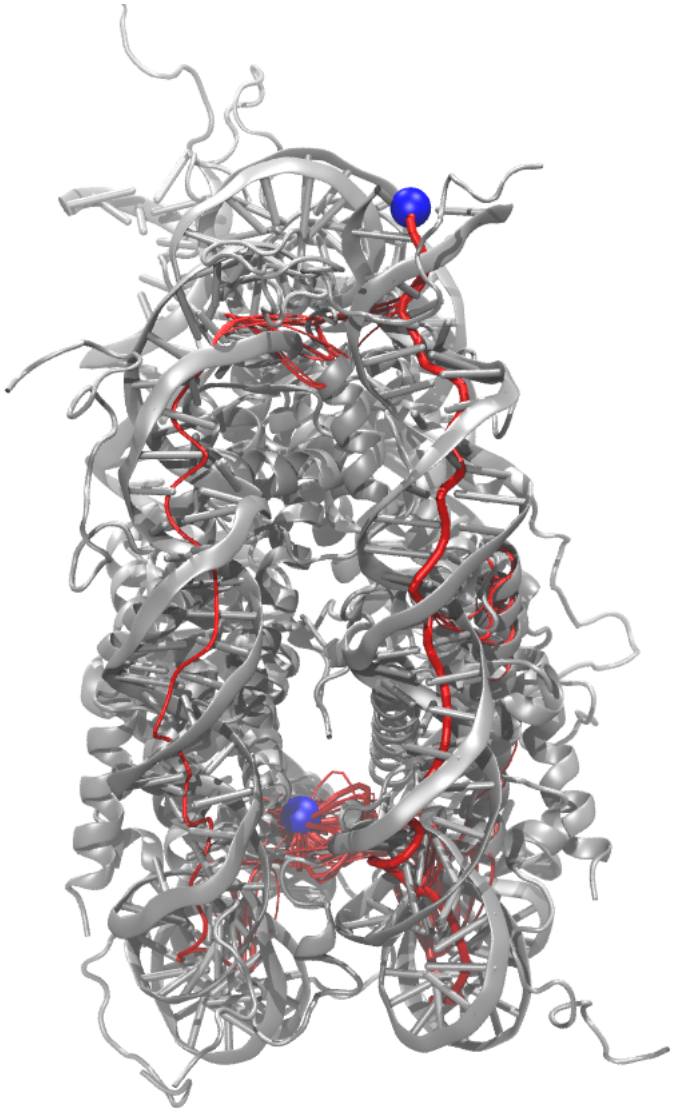

Figure S15: Sub-optimal pathways for L1 loop to DNA exit in the L1-Mutant nucleosome.

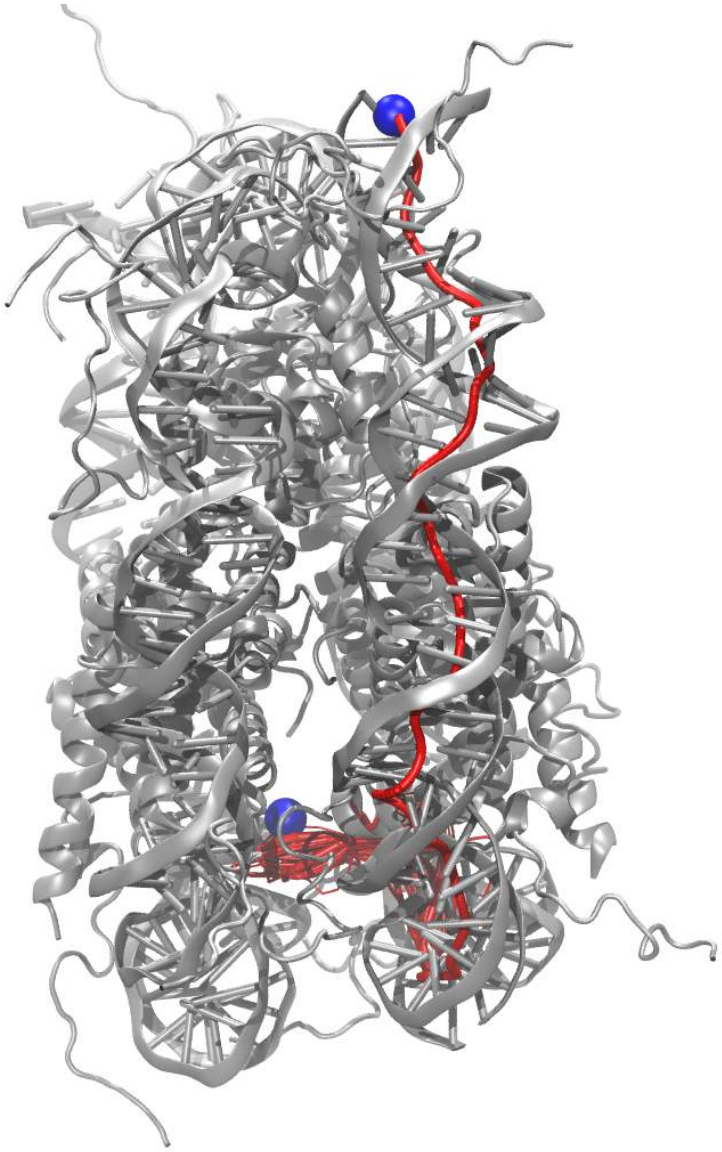

Figure S16: Sub-optimal pathways for L1 loop to DNA exit in the macroH2A nucleosome.

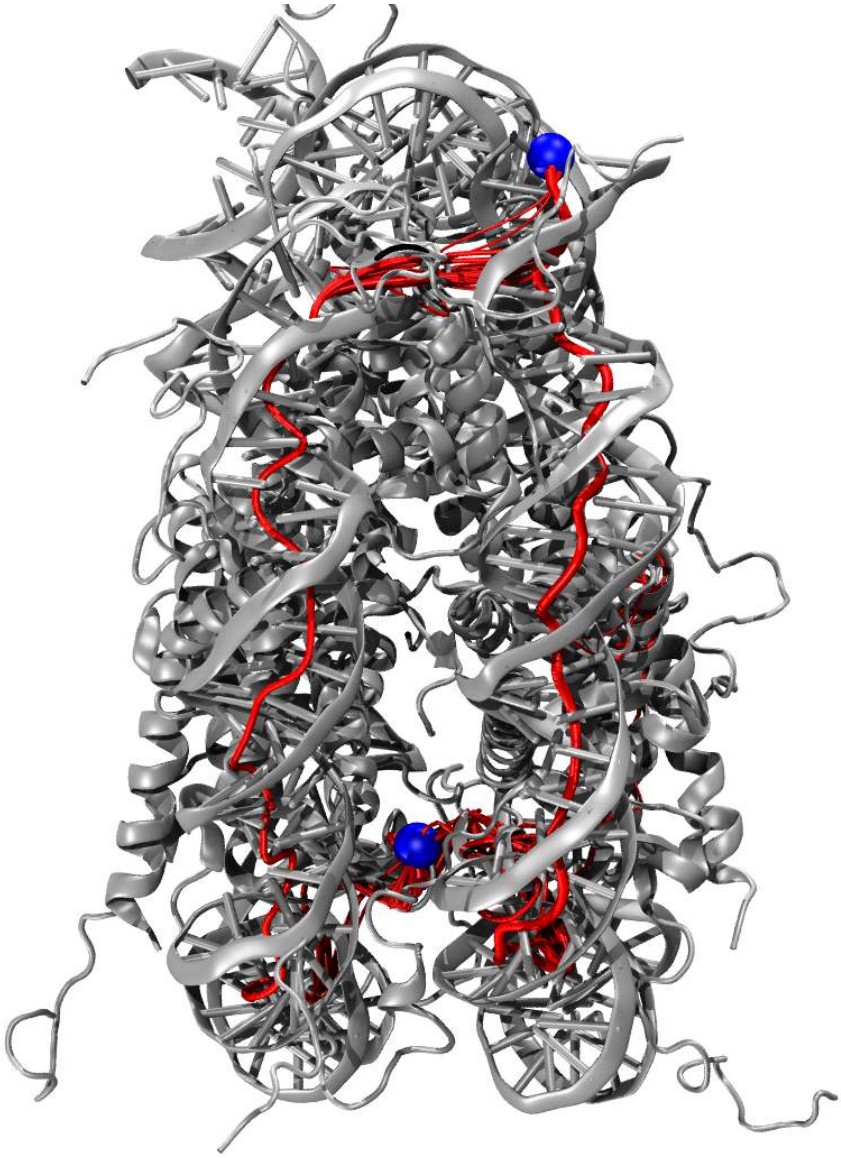

Figure S17: Sub-optimal pathways for L1 loop to DNA exit in the H2A.Z nucleosome.

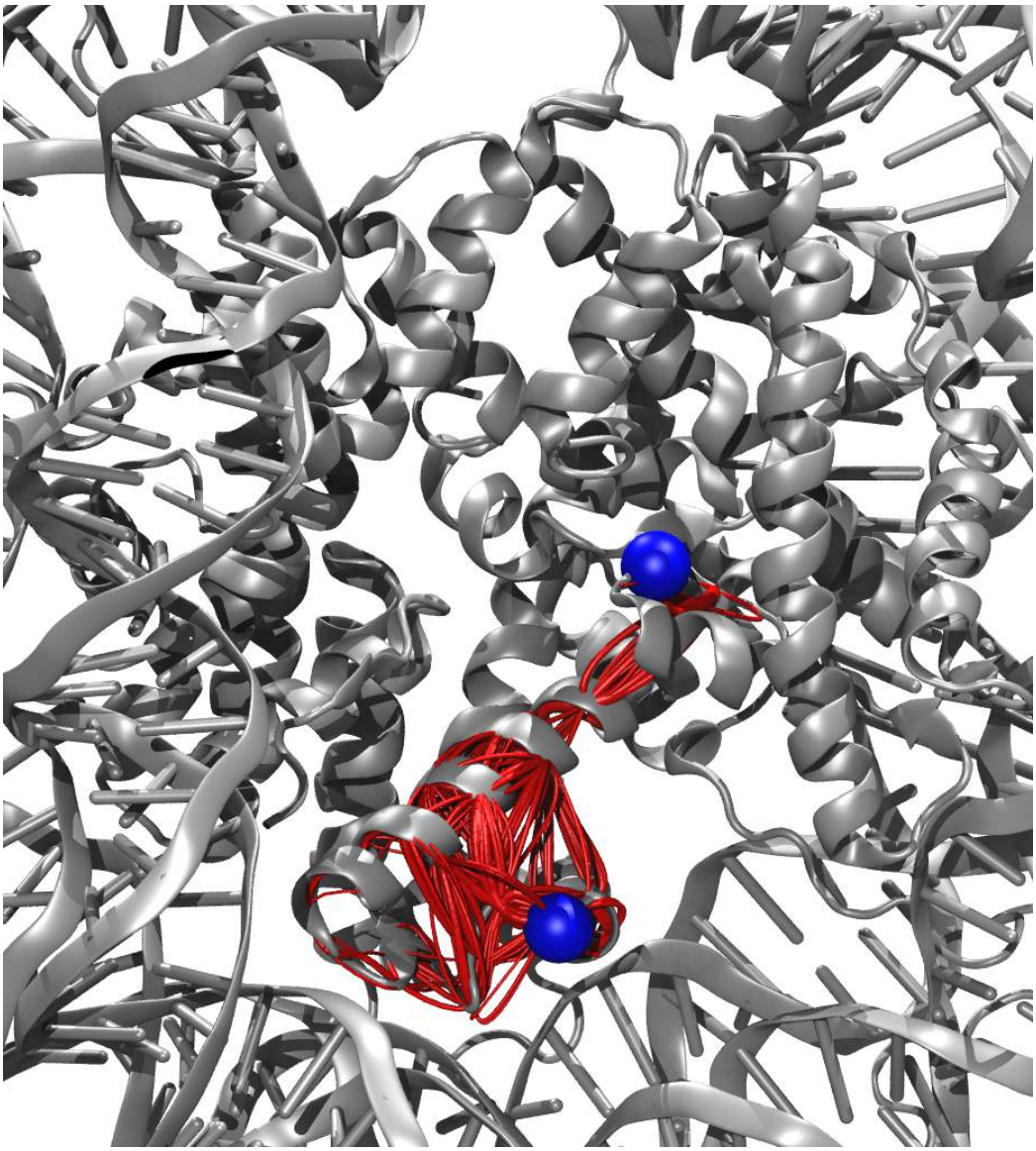

Figure S18: Sub-optimal pathways for L1 loop to the associated docking domain in the canonical nucleosome. The opposing dimer has been removed to improve visualization clarity.

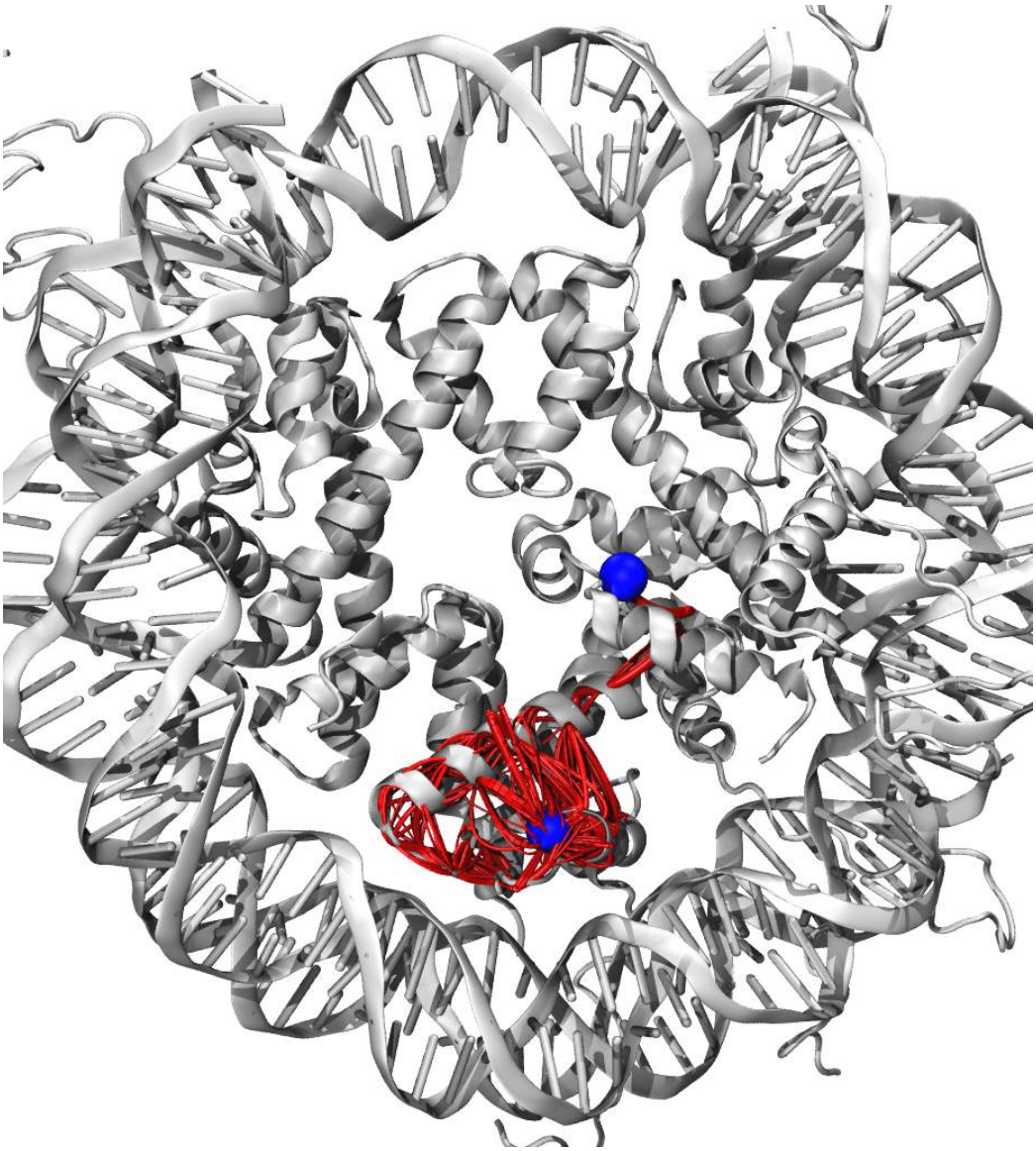

Figure S19: Sub-optimal pathways for L1 loop to the associated docking domain in the L1-Mutant nucleosome. The opposing dimer has been removed to improve visualization clarity.

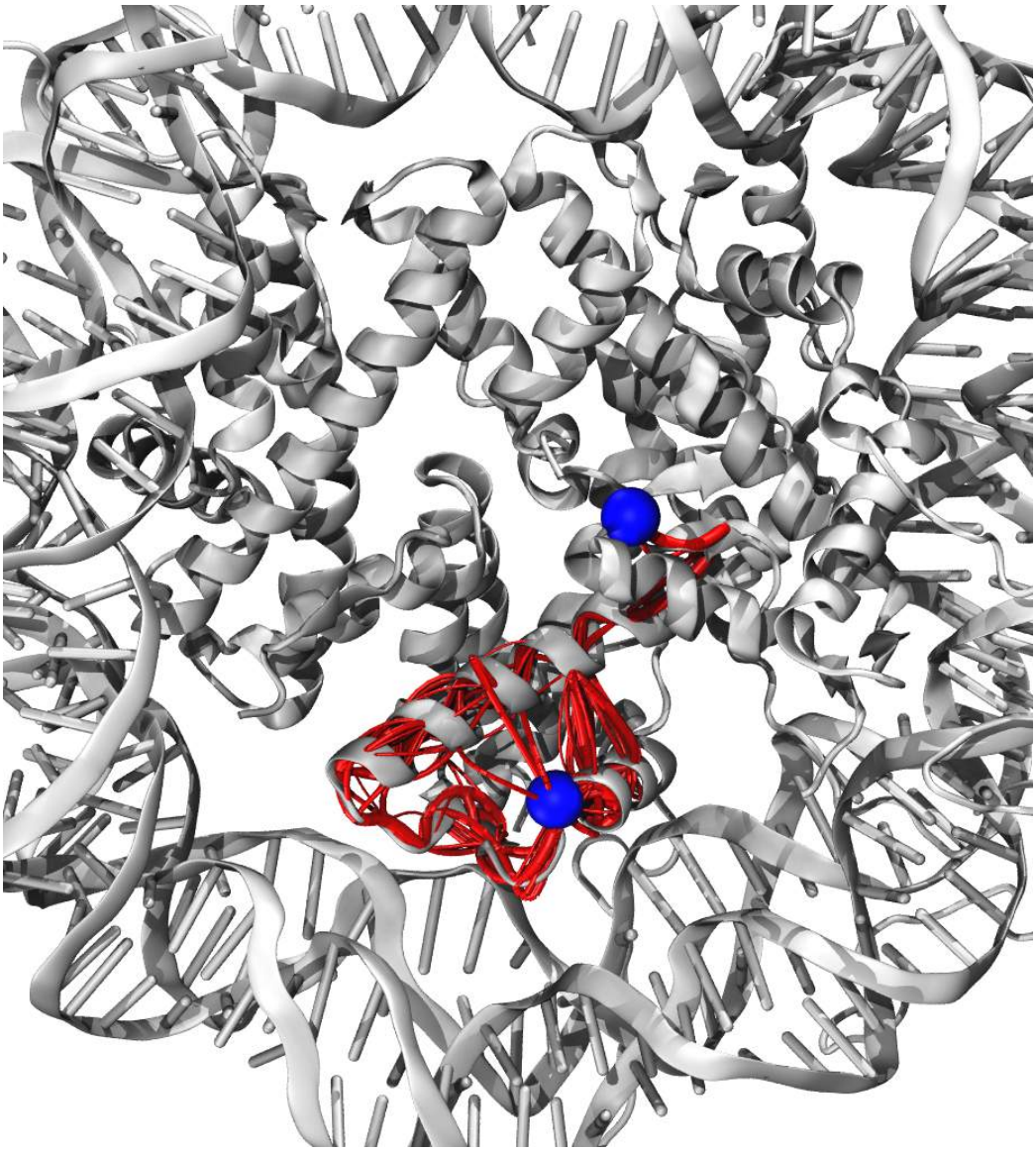

Figure S20: Sub-optimal pathways for L1 loop to the associated docking domain in the macroH2A nucleosome. The opposing dimer has been removed to improve visualization clarity

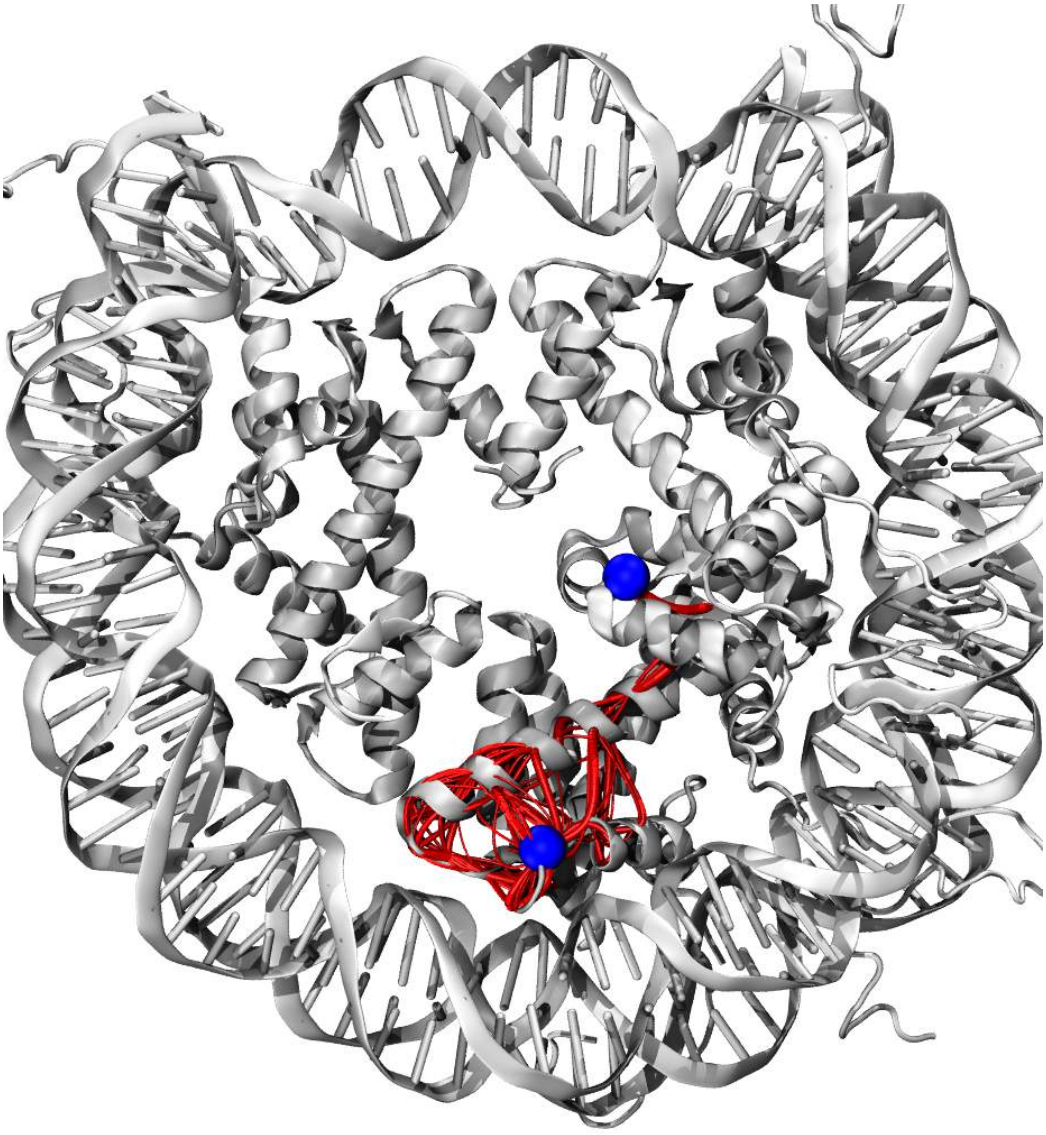

Figure S21: Sub-optimal pathways for L1 loop to the associated docking domain in the H2A.Z nucleosome. The opposing dimer has been removed to improve visualization clarity.

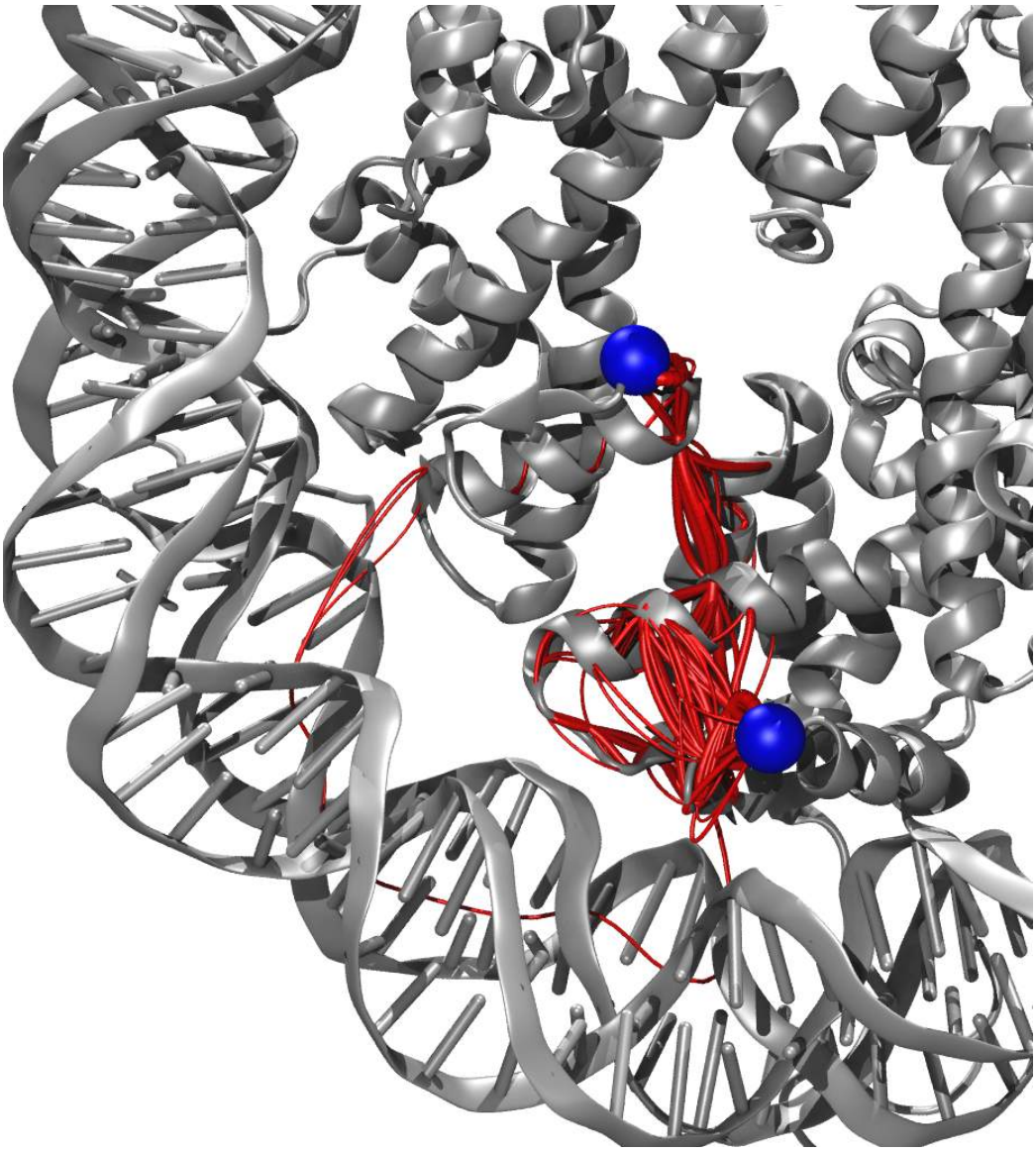

Figure S22: Sub-optimal pathways for L1 loop to non-associated docking domain in the canonical nucleosome. The opposing dimer has been removed to improve visualization clarity.

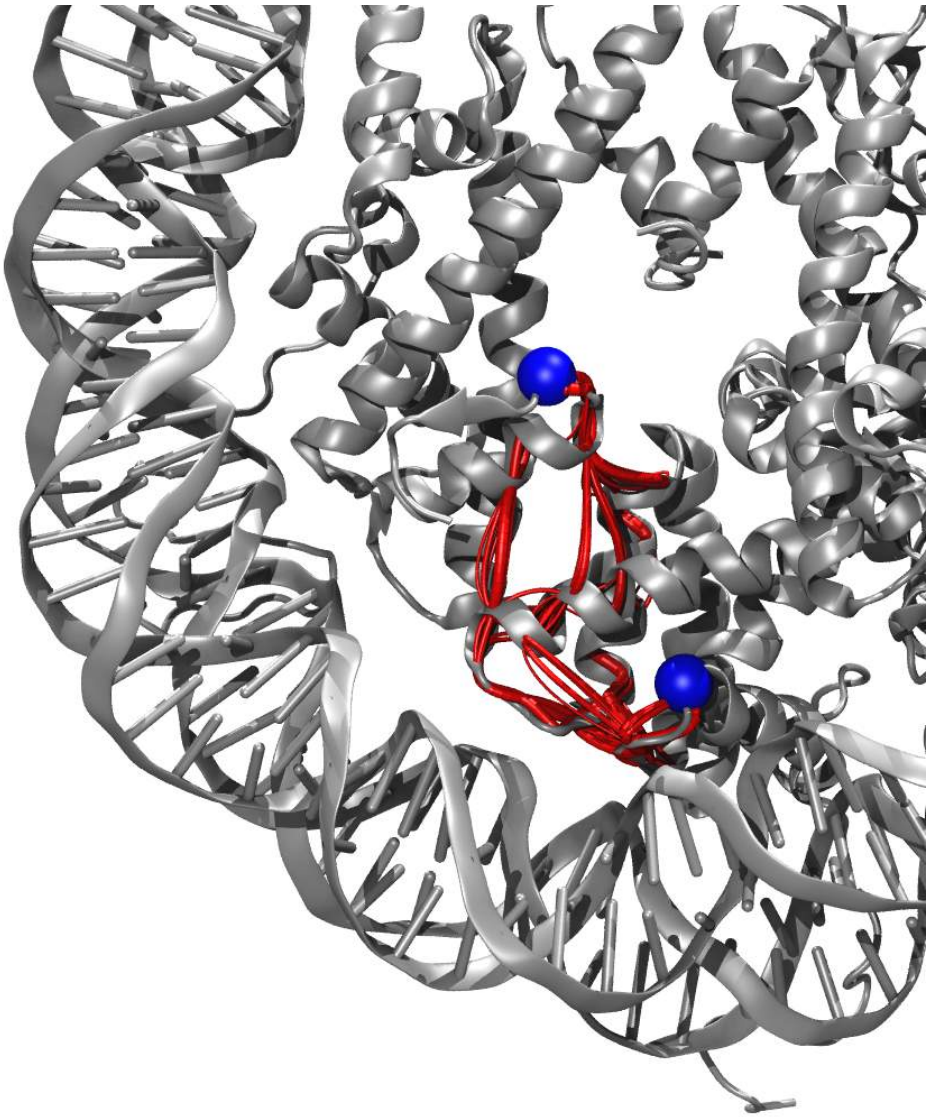

Figure S23: Sub-optimal pathways for L1 loop to non-associated docking domain in the L1-Mutant nucleosome. The opposing dimer has been removed to improve visualization clarity.

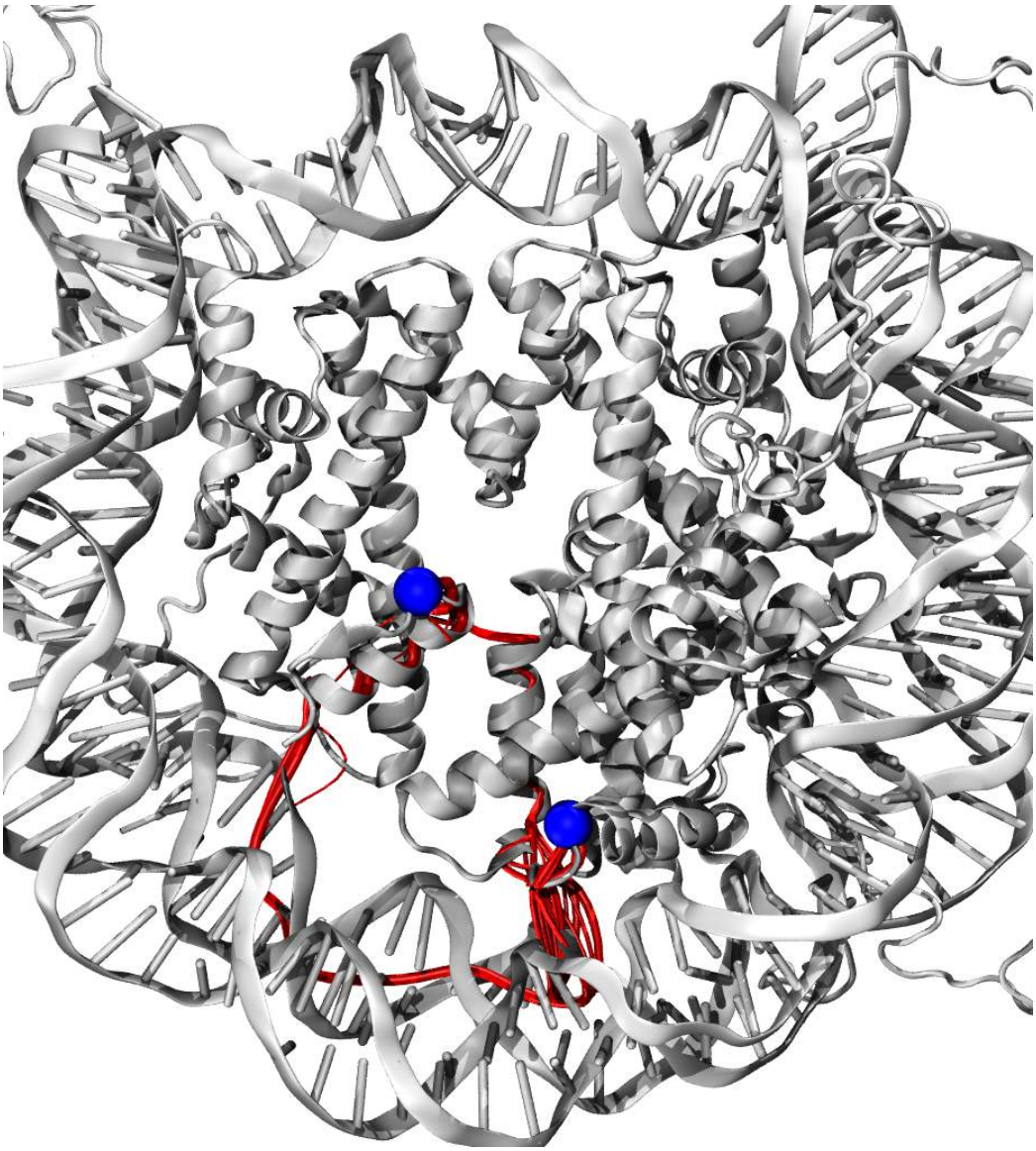

Figure S24: Sub-optimal pathways for L1 loop to non-associated docking domain in the macroH2A nucleosome. The opposing dimer has been removed to improve visualization clarity.

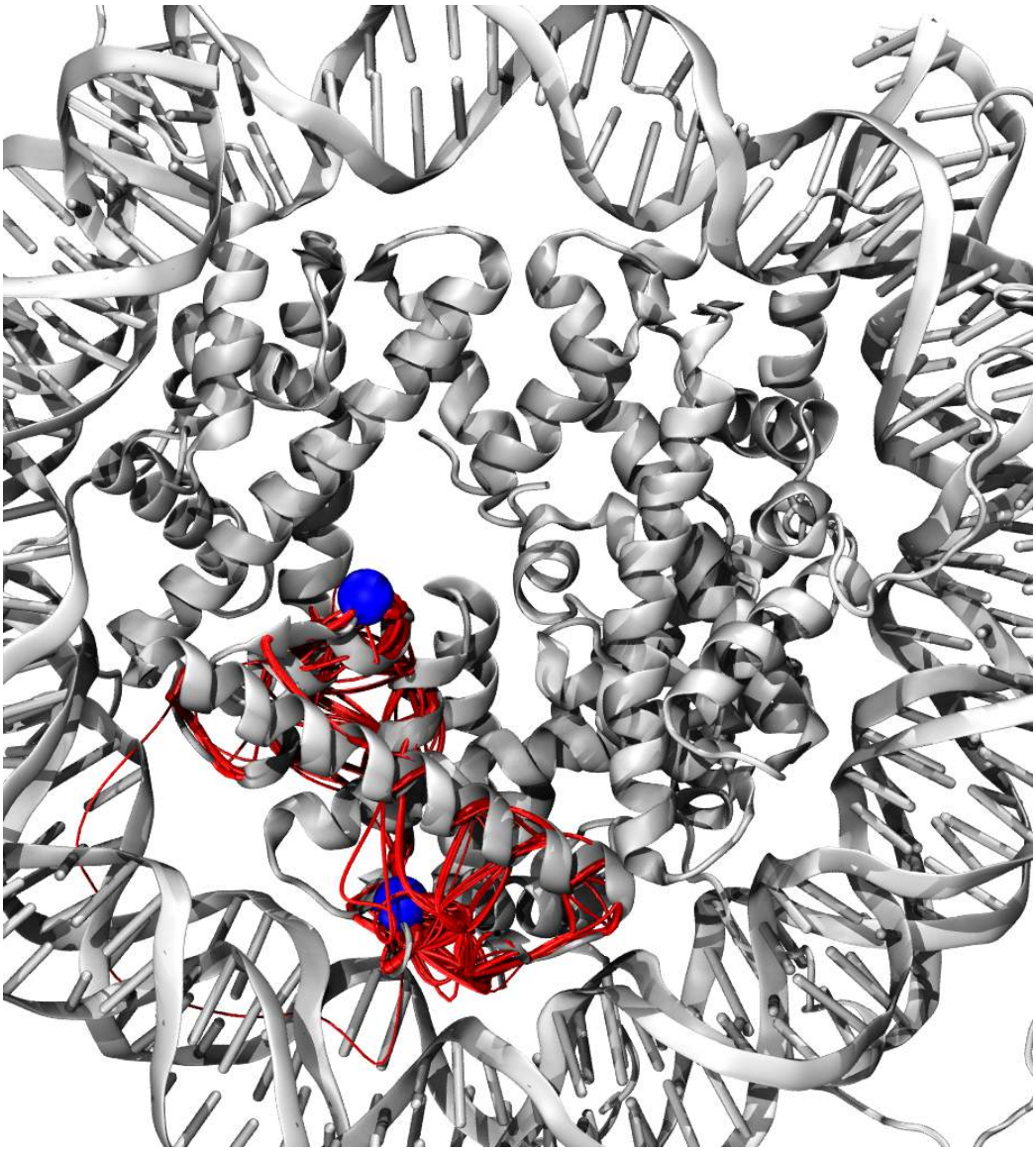

Figure S25: Sub-optimal pathways for L1 loop to non-associated docking domain in the H2A.Z nucleosome. The opposing dimer has been reduced to only H2B α2 to improve visualization clarity.